Fog Formation during Gravity Currents Interacting with Coastal Topography

Stef L. Bardoel[1] • Daniel V. Horna Muñoz[1,2] • Andrey A. Grachev[1,3*] • Raghavendra Krishnamurthy[1,4] • Leonardo P. Chamorro[5] • Harindra J.S. Fernando[1]

Received: DD Month YEAR/ Accepted: DD Month YEAR/ Published online: DD Month YEAR

Abstract An interesting mixing-fog event was identified during the C-FOG field campaign, where a cold front arriving from the north-east collided with the Downs peninsula in Ferryland, Newfoundland, to produce misty/foggy conditions. A comprehensive set of field observations suggests that this collision caused turbulent mixing of nearly saturated ambient air with an almost saturated cold front, creating conditions for mixing fog. To delve into physical processes underlying this phenomenon, laboratory experiments were performed on the interaction of lock-exchange induced gravity currents with a (rectangular) obstacle. Instantaneous velocity and density fields were obtained using particle image velocimetry and planar laser-induced fluorescence. The observations suggest that the obstacle starts affecting the approaching gravity-current propagation at an upstream distance of $2H$ and, upon collision, the mixing is taking place over a horizontal spatial extent of $0.83H$, where H is the depth of the ambient fluid layer. The time for larger-scale turbulent stirring to permeate to the smallest scales of turbulence and activate the

✉ Stef L. Bardoel
sbardoel@nd.edu

[1] Department of Civil and Environmental Engineering and Earth Sciences, University of Notre Dame, Notre Dame, IN, USA

[2] Department of Science and Centro de Investigación y Tecnología del Agua (CITA), Universidad de Ingeniería y Tecnología (UTEC), Barranco, Lima, Peru.

[3] NOAA Physical Sciences Laboratory / Cooperative Institute for Research in Environmental Sciences, University of Colorado, Boulder, CO, USA

[4] Pacific Northwest National Laboratory, Richland, WA, USA

[5] Department of Mechanical Science and Engineering, University of Illinois, Urbana, IL, USA

* Permanent Address: Boundary Layer Research Team/Atmospheric Dynamics & Analytics Branch, DEVCOM Army Research Laboratory, WSMR, NM, USA

condensation nuclei was estimated as $3t^*$, where $t^* = \sqrt{H/g'}$ is the intrinsic time scale of the gravity current and g' the reduced gravity. Extrapolation of laboratory results to field conditions showed a good agreement with observations.

Keywords C-FOG case study • Gravity currents • Mixing fog • Topography • Turbulent mixing

1 Introduction

Fog typically forms when air close to the earth's surface becomes slightly supersaturated and produces a layer of very small suspended water droplets (or clouds) in contact with the surface. The AMS Glossary (2020) defines fog in terms of visibility, a condition that reduces visibility below 1 km (0.62 miles). The extent of visibility reduction is considered as the 'intensity' of fog. The usual fog formation mechanism is the deposition of water vapour on hygroscopic aerosol nuclei (condensation nuclei CN) under favourable conditions, such as reduction of temperature that 'activates' CN leading to droplet growth (Gultepe et al. 2007). Dry atmospheric aerosols with a typical size of ~ 0.1 µm are small enough to scatter wavelengths of visible light preferentially, producing colours and give opalescent appearance to the atmosphere (known as haze, visibility 2-5 km). On the other hand, activated droplets are too large to yield differential scattering, lead to visibility impairment, and give a white appearance. These include mist (~ 1 µm, visibility 1-2 km) and fog (~ 1–30 µm, visibility < 1 km). There are many types of fog, three main types being radiation fog, advection fog, and mixing fog (Fernando et al. 2020). *Radiation fog* appears when net outgoing radiation cools the ground surface so as to drop the temperature of overlying air below the dew point. *Advection fog* (or *movement fog*, a term used when fog is localized) forms when relatively warm air overrunning a colder surface is cooled to saturation by air-surface exchange processes (warm fog) or cooler air moving over a warmer surface is saturated by evaporation (cold fog). Advection fog is not a feature of a particular synoptic type of wind speed regime. The mixing of two near-saturated air masses of different temperatures may produce supersaturation and, therefore, *mixing fog* (Taylor 1917), which is the focus of this paper.

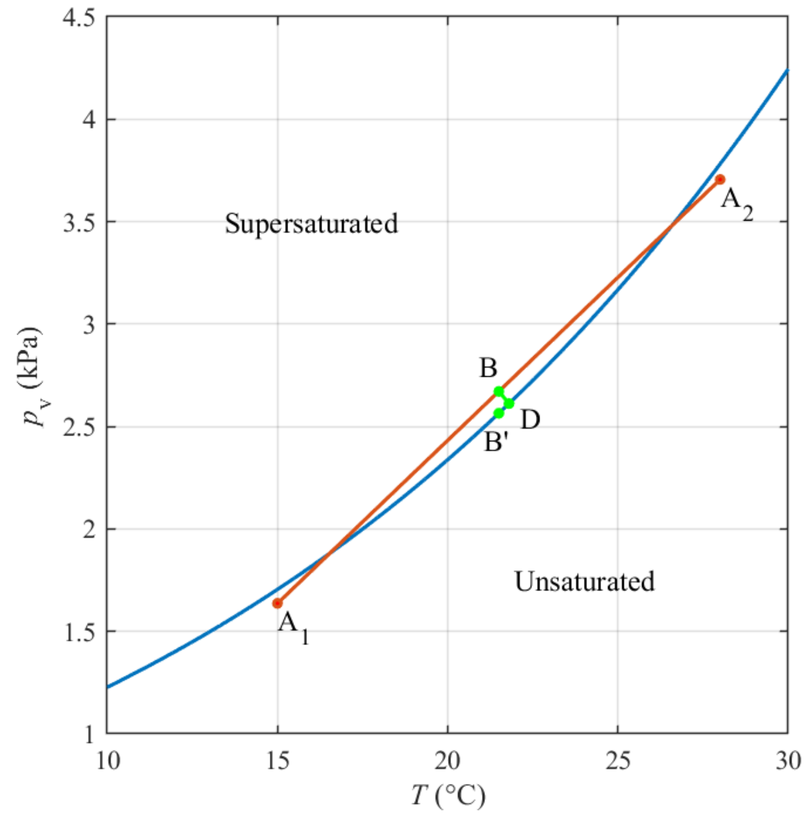

Fig. 1 A diagram of water vapour (partial) pressure as a function of temperature, illustrating the mixing of moist air masses A_1 and A_2 to produce fog at B

The mechanism of mixing-fog formation is best explained using the curvature of the water vapour pressure p_v (ordinate) and temperature T (abscissa) diagram (Rhode 1962), as illustrated in Fig. 1. The blue line represents the saturation vapour pressure p_s curve for water vapour, which is described by the Clausius-Clapeyron equation for a perfect gas $d(\ln p_s)/dT = L(T)/RT^2$, where $L(T)$ is the latent heat of evaporation, which is a function of T, and R the universal gas constant. Air parcels located to the left of this curve are supersaturated and to the right are unsaturated. The mixing line of two near-saturated air masses of different temperatures (A_1 and A_2) is shown in red, and in favourable situations of mixing the two air masses lead to B, which is supersaturated and preconditioned for fog (for a derivation of mixing line for a special case, see Schumann 1996). The liquid water content (*LWC*) of B can be estimated by considering the difference of water vapour pressure of point B and the saturation water vapour pressure B' at the same temperature. However, due to the release of latent heat, the temperature of air-mass state B increases during condensation and may reach D instead. Therefore, the overall mixing process is nonlinear and the *LWC* is determined by the difference in water vapour pressure of points B and D. Fog is expected when the mixing curve traverse to the left of the saturation curve, and the appearance is more of cirrus nature. Persistence of fog requires that the state of the final mixture is to the left of the saturation curve, otherwise fog is short lived (Paoli and Shariff 2016).

It is also noted that the depiction in Fig. 1 does not consider the droplet activation by CN, which may occur under unsaturated or supersaturated conditions (Gultepe et al. 2007). An interesting aside is the case where A_1 and A_2 are further apart, as in the case of a humid jet engine exhaust in colder air in the upper atmosphere. In such cases, the mixing line first crosses the saturation curve of ice, and then into the supersaturation to produce contrails when the so-called Schmidt-Appleman criterion is satisfied (Paoli and Shariff 2016). The thread of the argument leading to this criterion is analogous to mixing-fog formation, except that the airmasses involved are in a different p_v-T regime and thus physical processes at play can be different.

An example is mixing fog that forms during the meeting of warm or cold masses at a front. Byers (1959) defined three fog categories related to fronts, namely pre-frontal, post-frontal, and frontal-passage. Pre-frontal fog occurs before a warm front, whence warm rainfall evaporates into colder air close to the ground and increases humidity toward saturation. Post-frontal fog shortly follows the passing of a cold front, also due to evaporation of rain. Fog behind a cold front, however, is not as widespread because precipitation bands of cold fronts have smaller spatial scales (Gultepe et al. 2007). The third and of interest to this paper is frontal-passage fog, which occurs during the mixing of nearly saturated cold and warm air masses (e.g. Fig. 1). Petterssen (1941) noted that it is impossible to form dense fog by mixing alone, because of the relatively small amount of condensation during mixing. According to Roach (1994), however, dense mixing fog is possible when the temperature difference between the warm and cold air masses is ~ 10°C. The formation of dense fog is also abetted by radiative cooling. George (1940) noted that enhanced mixing of air masses at rough terrain increases the likelihood of fog. Thus, in order to successfully predict coastal mixing fog, it is crucial to understand the interaction of fronts with coastal topography.

Cold fronts belong to the class of flows driven by density differences or gravity currents. Numerical models of gravity-current/obstacle interactions have been developed for both 2D and 3D cases (Gonzalez-Juez and Meiburg 2009; Tokyay et al. 2012; Nasr-Azadani and Meiburg 2014; Tokyay and Constantinescu 2015; Jung and Yoon 2016; Nasr-Azadani et al. 2018), mostly focussing on confined and unconfined turbidity currents, with model validations conducted against laboratory data. Theoretical developments have been made using shallow water models (Rottman et al. 1985; Lane-Serff et al. 1995), but these models are incapable of rapid transient flow adjustments and mixing at the obstacle. The influence of background rotation on gravity currents with and without sloping surfaces has been studied numerically and using linear and non-linear theories (Hunt et al. 2005) and laboratory experiments (Mahalov et al. 2000). The influence of background turbulence and bottom (surface) friction on gravity current frontal mixing has been modelled by Noh and Fernando (1991, 1993). Nevertheless, experimental laboratory studies on gravity currents interacting with topography have been sparse. Lane-Serff et al. (1995) studied the interaction of a gravity current with a triangular obstacle, where the flow was found to split at the obstacle to a reflected hydraulic jump and an overflow at the obstacle. More recently, Wilson et al. (2018, 2019) performed experimental studies on the interaction of lock-exchange generated gravity currents with a rectangular obstacle. Measurements of instantaneous velocity fields using ultrasonic Doppler velocity profilers showed that velocity profiles in the unobstructed currents have a log-Gaussian shape. In contrast, those of obstructed flow close to the obstacle are more Gaussian. Downstream of the obstacle, the maximum velocity and turbulence intensity were 48% and 28%, respectively, less than unobstructed experiments; i.e., the obstacle decreased the downstream current's maximum velocity and turbulence, possibly by vertical spreading of turbulence activity and due to enhanced dissipation. The height and variance of the maximum speed and turbulence were larger at the obstacle, suggesting its possible role in enhanced mixing and entrainment of ambient fluid into the gravity current.

The present study was motivated by field observations of the "Toward Improving Coastal Fog Prediction" (C-FOG) project (Fernando et al. 2021), which included twelve land-based and three ship-based Intensive Operational Periods (IOPs). An interesting, conceivably a mixing-fog, event occurred during IOP7 (0000 UTC 16 September to 1430 UTC 17

September 2018), where a cold front from the north-east collided on a peninsula (Downs promontory in the town of Ferryland) protruding into the Atlantic Ocean. It is hypothesized that this collision caused warm near-saturated ambient air to mix with colder near-saturated air at the cold front, thus producing mist and fog. In this paper, the observations from IOP7 will be presented in Section 2, together with a description of the observational area and field measurements. Given sparse previous observations on turbulence generated by a gravity current impinging on a topography, a laboratory experiment was conducted to study the impingement of a lock-exchange released gravity current on a rectangular obstacle. The experiment is described in Section 3, followed by results in Section 4 and a discussion in Section 5. The conclusions are given in Section 6.

2 Field Observations

The C-FOG field program involved measurements in eastern Canada at three main coastal land sites on the Avalon Peninsula, Newfoundland (NL) and one in Nova Scotia (NS). Additionally, measurements were conducted aboard an instrumented research vessel R/V, Hugh R. Sharp, that tracked on the coastal areas of NL and NS. The fog-climatology based site selection and the details of the C-FOG field program, including IOPs, are given in Fernando et al. (2021). The information given below is relevant to IOP7 only.

2.1 Instrumentation

During IOP7, the Ferryland site registered relatively short fog events, while other land sites or the R/V did not record fog. The Ferryland site consisted of three auxiliary sites, the Downs site (mentioned earlier, 32 m above sea level a.s.l.), Battery site (3 m a.s.l.), Beach House site and Judges Hill site (129 m a.s.l. on a nearby hill). Downs and Battery were the two most densely instrumented. Figure 2 is a visual overview of the Ferryland sites.

Figure 3 shows the instrumentation at the Downs and Battery sites used for this study. The Downs site had a 16.2 m tower with four levels (2, 5, 10 and 15 m above ground level a.g.l.) of instrumentation, with each level having a fast response three-axis ultrasonic anemometer (Model 81000, R.M. Young) for velocity components and virtual temperature at 20 Hz and four slow response HC2S3 (Campbell Scientific) temperature and relative

Fig. 2 Overview of Ferryland C-FOG sites

humidity (T/RH) measurements at 1 Hz. The tower also had a LI-COR Inc. fast response (20 Hz) open-path infrared gas analyzer (LI-7500A) for water vapour fluxes mounted at 5 m. The visibility was measured by a Present Weather Detector (PWD22, Vaisala Inc.), with data recorded at every 15 s. Other details of the turbulence measurements, data processing, and data-quality criteria for the measurements at Downs during the C-FOG field campaign can be found in Grachev et al. (2018, 2021). The site also had a Scintec MFAS SODAR/RASS wind and temperature profiling system as well the Naval Postgraduate School (NPS) Aerosol Sampling Unit (NASU) microphysics trailer housed with a modified

CDP-2 (Droplet Measurement Technologies) for cloud/fog droplet size spectrum (2-50 μm) measurements. Two Halo Photonics Streamline XR Doppler lidars, at the Downs and Battery sites, were conducting co-planar range-height indicator scans to measure winds and aerosol backscatter. The dual doppler configuration setup and general lidar info is described by Newsom and Krishnamurthy (2020) and Vassallo et al. (2021).

The instrumentation at the Battery site included a CL31 ceilometer (Vaisala Inc.) that measured aerosol backscatter for cloud base height (CBH) or fog extent observations. There was also a Present Weather Detector (PWD52, Vaisala Inc.) for visibility measurements and a camera that took a photo of the Downs once every five minutes. Judges Hill had a PWD22 (Vaisala Inc.) for visibility measurements. The Beach House site had

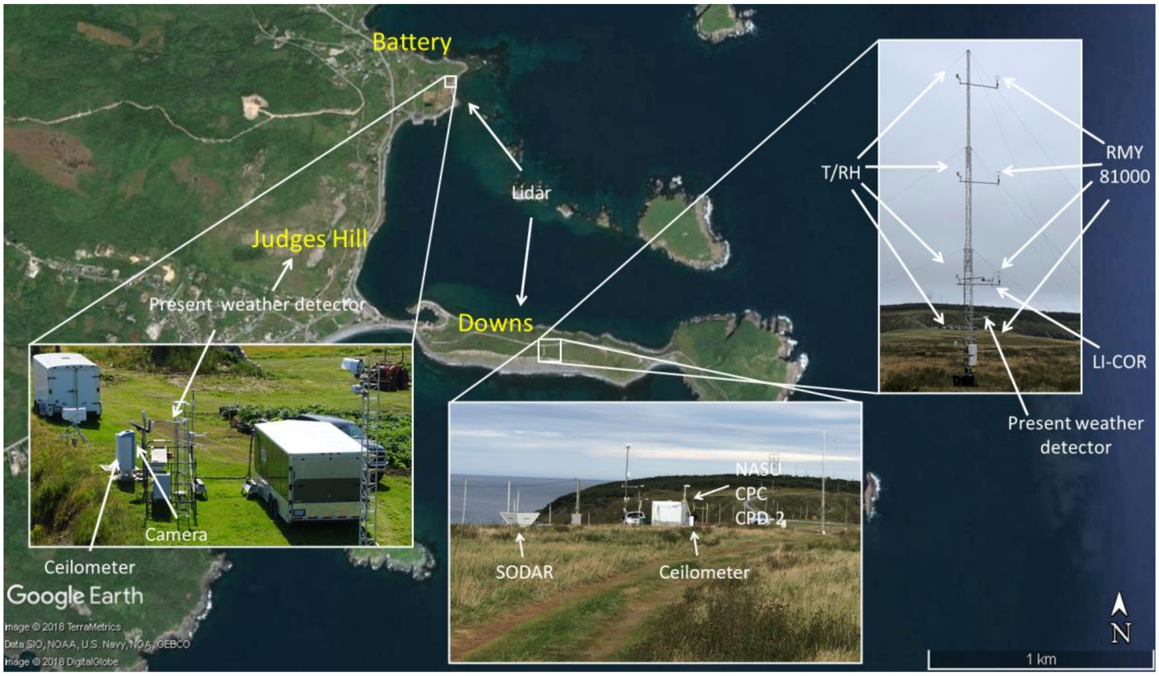

Fig. 3 Instrument map of the Ferryland sites: the Downs, Battery, Judges Hill. Details of the instrumentation are given in the text

only a scanning Doppler Lidar.

2.2 Fog observations during IOP7

At 0000 UTC 16 September (local time = UTC – 2.5 h) the winds were westerly and ~ 10 m s^{-1}. The wind speed steadily decreased to ~ 2.5 m s^{-1} until 0900 UTC and remained constant until 1130 UTC (to be shown later, Fig. 7a). The visibility of all Ferryland sites observed by PWDs was similar until this time (Fig. 4a) but then started to drop at all stations. At ~ 1200 UTC, fog/mist appeared at the low-lying coastal stations (Downs and Battery) with visibility teetering around and dropping below 1 km. The *LWC* and the droplet number concentration N_d at Downs first spiked at the time of first fog/mist occurrence and then dropped somewhat until 1300 UTC where visibility dropped again and *LWC* and N_d increase (Fig. 4b,c), with the appearance of fog/mist again. The mean droplet diameter also increased from 4 to 6 µm at ~ 1200 UTC (Fig. 4d). This agrees well with a study conducted on the Californian west-coast (Goodman 1977), where coastal fog was observed to have a mean droplet diameter ranging from 4.5 to 10 µm. Inspection of ceilometer backscatter (Fig. 4f) and the observations described below show that there is an intense mixing event starting at ~ 1145 UTC but without a clear cloud ceiling even after

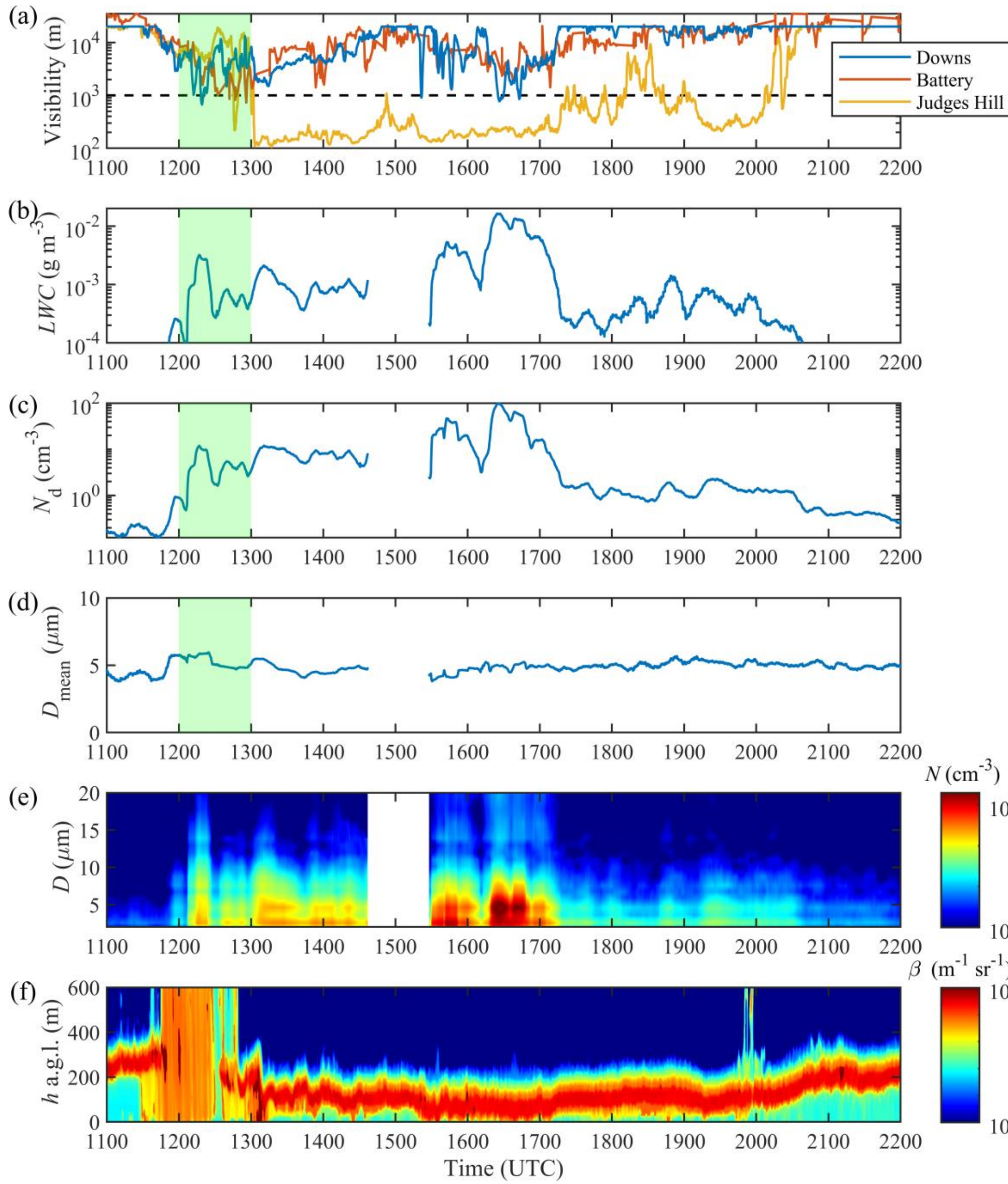

Fig. 4 Time series of (a) visibility, (b) liquid water content, (c) droplet number density, (d) mean droplet diameter, (e) droplet number density spectrum, and (f) ceilometer backscatter profile during IOP7 (16 September 2018). The visibility was measured with a PWD, the backscatter profile with a ceilometer, and the other variables are measured with a CDP-2

the appearance of fog at 1200 UTC and until about ~ 1230 UTC (ceilometer at the Downs malfunctioned, and hence data from the Battery site is shown). In Fig. 4f, there appears to be a stratus cloud layer from 200-300 m prior to the event, and there is no gradual cloud

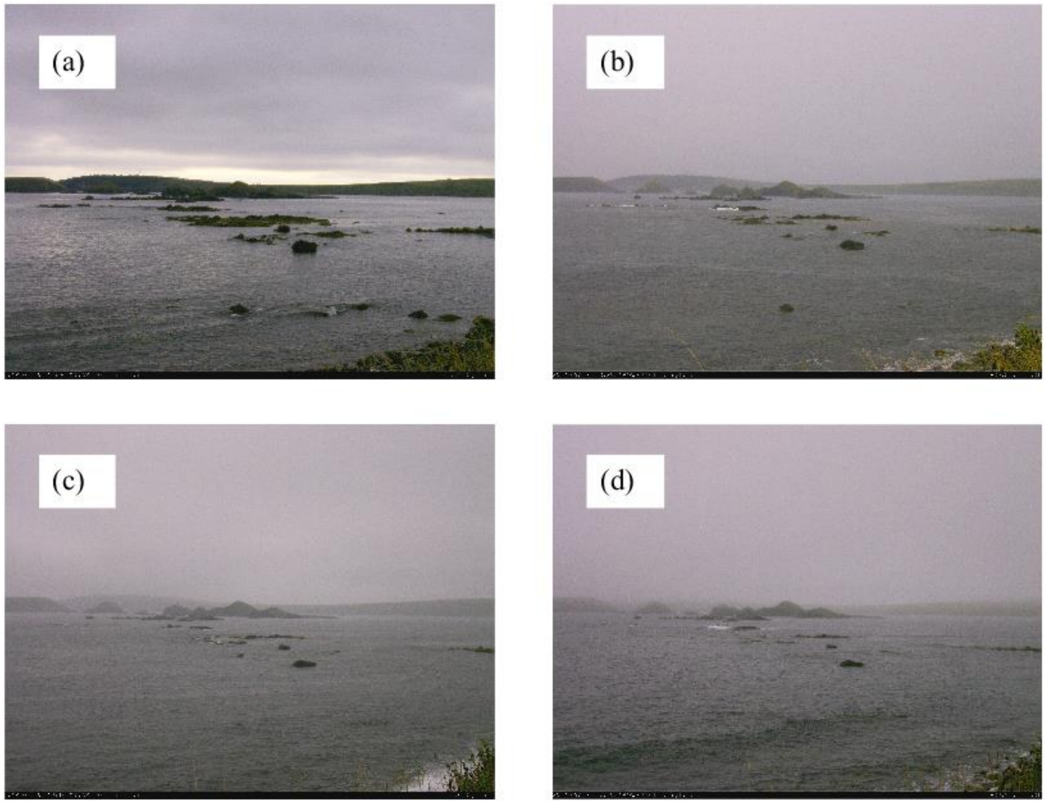

Fig. 5 Visibility observations at Downs during IOP7 (16 September 2018); photos from a camera at the Battery site at time (a) 1100 UTC, (b) 1220 UTC, (c) 1310 UTC, (d) 1640 UTC

lowering leading to the event; instead, an abrupt mixing event appeared, following which the cloud layer re-established, whereupon another mixing event followed at 1300 UTC. Visual observations by a camera directed at Downs also confirmed a fog layer with a diffused top (Fig 5b,c). Range-corrected backscatter profiles from Doppler lidars give a view of the fog event. A scan taken at 1215 UTC shows the presence of a fog layer that is ~ 45 m thick above Downs (Fig. 6b).

The cloud base height was approximately 270 m a.s.l. or 240 m a.g.l. (Fig. 6a). The vertical mixing evident spanning the entire air column above Downs Topography evident in Fig. 4f is not clear here, but a fog layer over Downs and the remnant cloud layer are very clear. Since Doppler lidars were scanning at an angle away from Downs, the Doppler lidar beams were not attenuated as observed by the ceilometer measurements (vertically pointing) in Fig 4f. Overall, the results suggest that the fog event observed in IOP7 is not due to stratus lowering. Tower data at Downs indeed confirmed the occurrence of an intense turbulent mixing event at 1145 UTC with (i) a gradual change of winds from westerly to north-

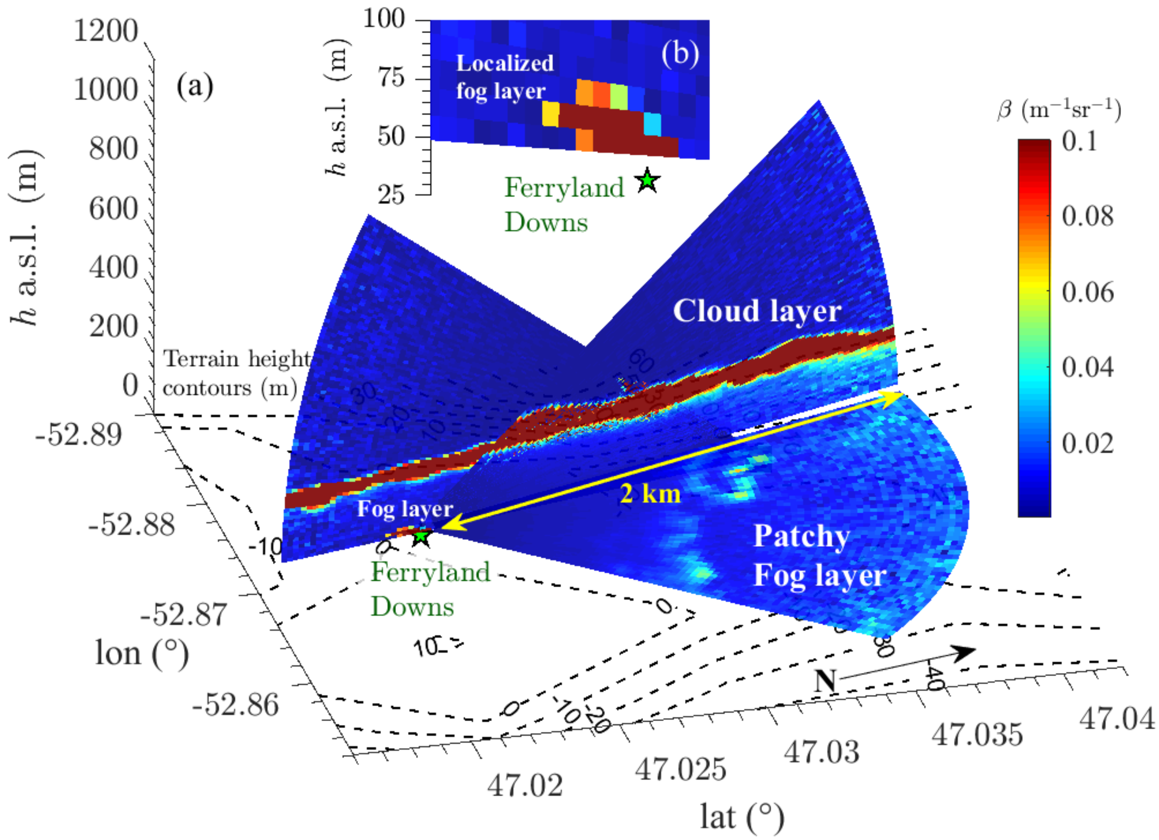

Fig. 6 Range-corrected backscatter from Doppler lidars located at Downs and Battery sites at 1215 UTC during IOP7 (16 September 2018). (a) shows range-corrected backscatter profiles for the entire range of the lidars, and (b) inset shows a zoomed section of backscatter measurements above Downs. The fog layer above Downs is about 45 m thick. The base of the cloud layer is ~ 270 m a.s.l. The dashed contours represent the terrain height in m. (adapted from Fernando et al. 2020)

westerly with a temporary gust and then stagnation during 1215-1300 UTC (Fig. 7a,b); (ii) a gradual drop of near-surface *T* (Fig. 7c); (iii) an increase of *RH* (Fig. 7d); and (iv) increase of turbulent kinetic energy (*TKE*), its dissipation rate (ε) as well as the *rms* temperature fluctuations (σ_θ) (Fig. 7e,f,h). No significant changes of surface heat flux occurred except at the two lowest levels indicating momentarily large negative fluxes, perhaps due to undercutting of a cold front as a paint stripper and raising colder air past the sensors (Fig. 7g). All these observations are consistent with the possibility of a local turbulent mixing event produced by mixing of two air masses of near saturation (existing air mass *RH* ~ 94%, after mixing rising to ~ 98-100%) that produced fog. The temperature difference between the airmasses was ~ 4°C. The absence of fog at the Judges Hill site during the event confirms that this is a local event confined to lower altitudes (and unrelated to

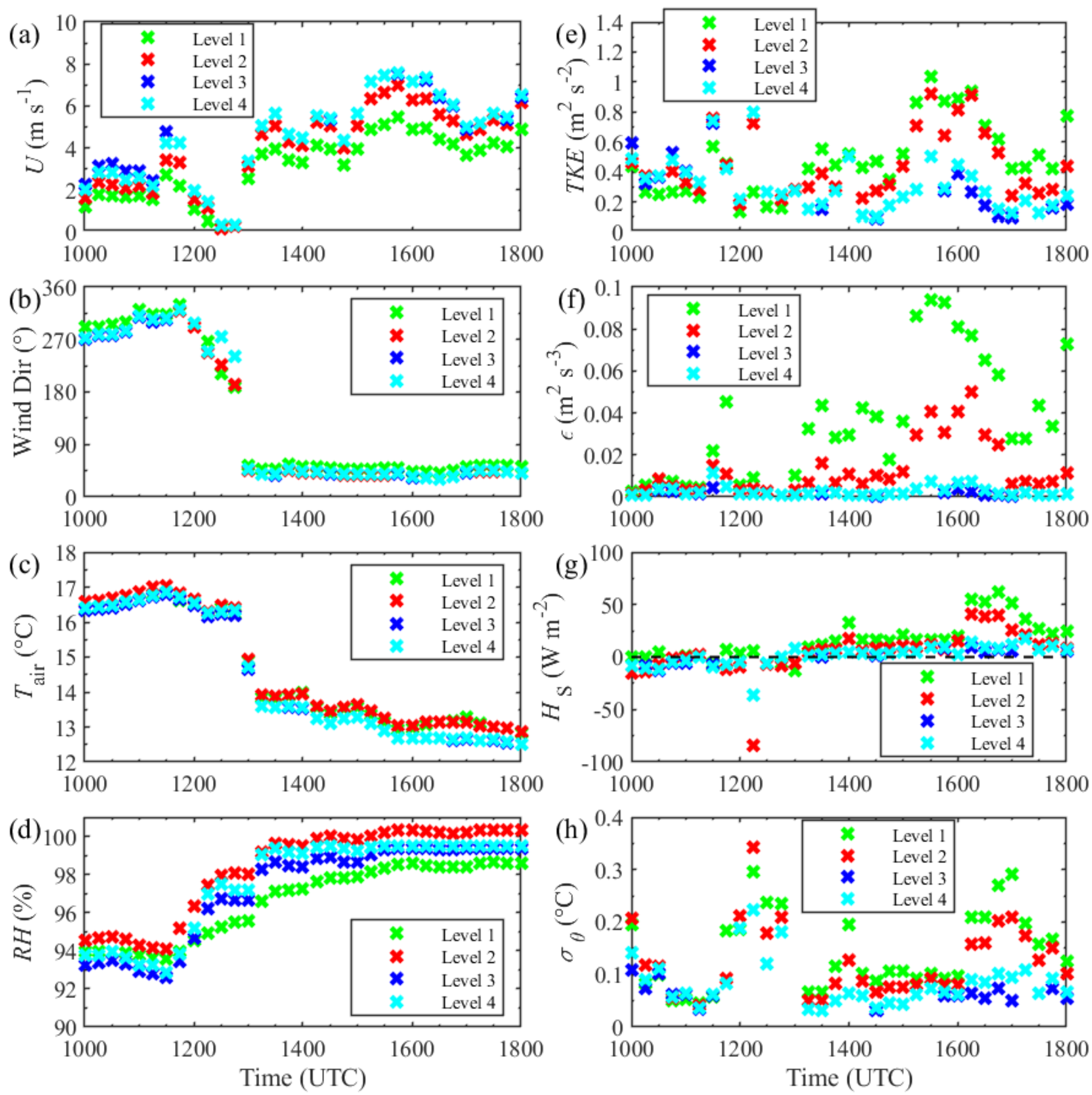

Fig. 7 Time series of (a) wind speed, (b) wind direction, (c) air temperature, (d) relative humidity, (e) *TKE*, (f) *TKE* dissipation rate, (g) sensible heat flux and (h) standard deviation of sonic temperature. The data was collected from a 16.2 m flux tower at Downs with four levels during IOP7 (16 September 2018). The wind speed, wind direction, and turbulence statistics are calculated from 15-min averaged 20 Hz ultrasonic anemometer measurements. Temperature and relative humidity were measured using 1 Hz T/RH sensors. Four levels are 2 (level 1), 5 (level 2), 10 (level 3) and 15 (level 4) m a.g.l. (also see Fernando et al. 2020 and Grachev et al. 2021)

possible stratus lowering) at least during the stagnation event (1215-1300 UTC). We hypothesize that a north-easterly cold front arriving approximately along the coast and impinging on the headland protruding to the ocean is a possible cause for this event. The appearance of fog ~ 15 minutes after the initiation of the event at 1145 UTC supports the

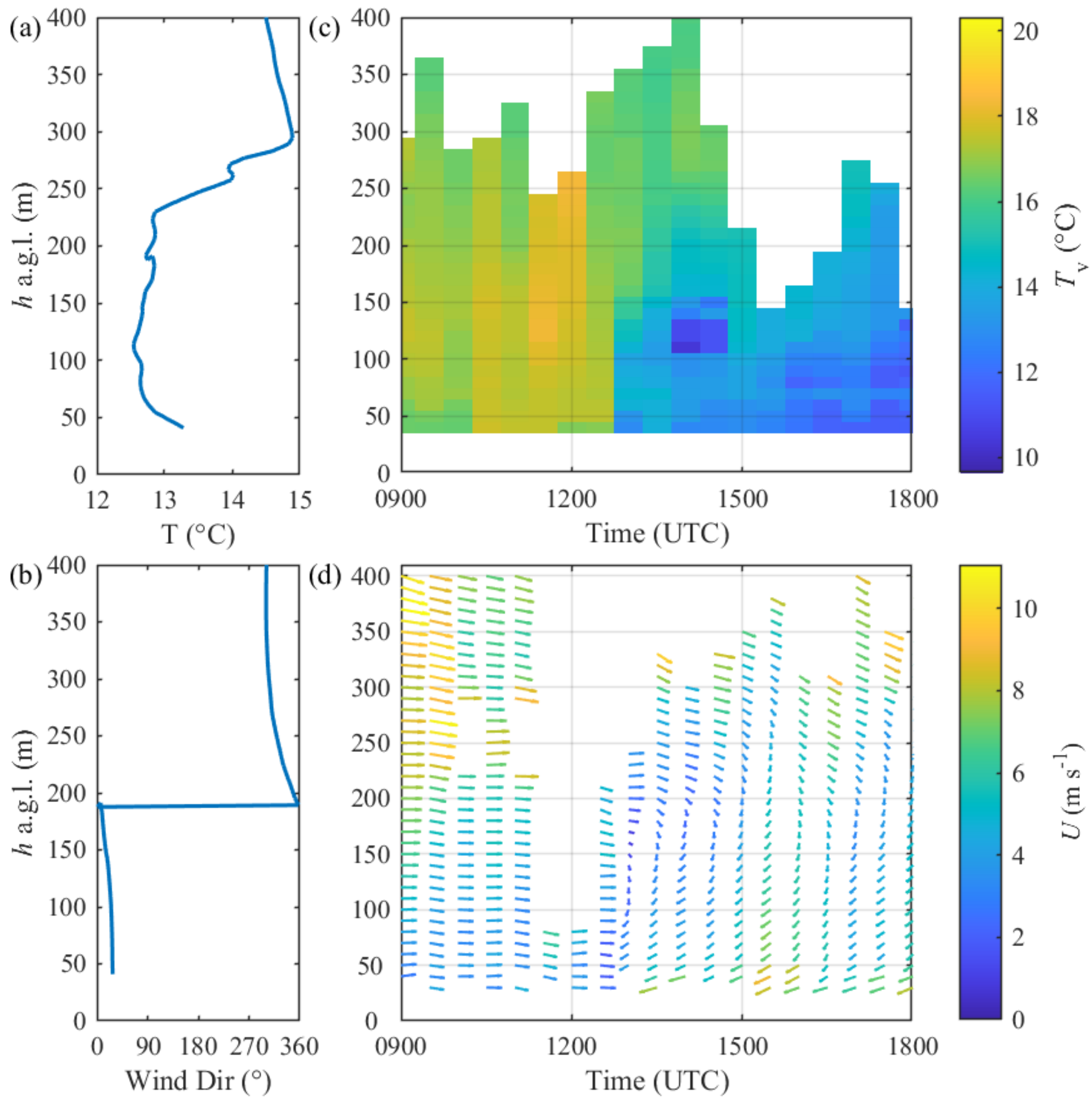

Fig. 8 Vertical profiles during IOP7 (16 September 2018) of (a) temperature and (b) wind direction as measured by a radiosonde. The profile was taken at 1445 UTC at the Downs site. SODAR/RASS profiles of (c) virtual temperature and (d) wind vectors from the Downs site

idea that this is a mixing fog event, since the event is triggered during the arrival of frontal intrusion at the Downs topography, wherefore turbulent mixing is initiated. Thereafter some time is needed for frontal-scale mixing to permeate to microphysical levels to spawn fog at sub-Kolmogorov scales. This will be addressed using a laboratory experiment later.

A somewhat broader perspective of the above event could be obtained using Sodar/RASS measurements at Downs. This system measures wind components and temperature above

~ 30-40 m, and 30 min averaged wind vectors and temperature are shown in Fig. 8c,d. The Sodar/RASS registered a change of winds to north-easterly after 1300 UTC, indicating that the changes of wind velocity at lower levels at 1130 UTC in Fig. 7a,b is due to the arrival of the shallow gravity current nose at ~ 1145 UTC, followed by a trailing current of greater thickness (for a review, see Simpson 1999). The front impinges on the Downs topography, stagnates momentarily during the flow adjustment, accelerates due convergence over topography, and causes mixing at low levels (Fig. 7). The turbulent front is then advected past the topography, establishing a quasi-steady trailing current, which appears to occur at ~ 1300 UTC. This transition is evident from wind velocity and T records in Figs. 7a,b and 8, which show a flow establishment at ~ 1300 UTC. From Sodar/RASS data (Fig. 8c,d), it appears that the thickness of the trailing gravity current, estimated using the height where T drops to background values, is about ~ 200-250 m, which is in agreement with the radiosonde launch made at 1445 UTC shown in Fig. 8a,b.

To further investigate whether intense mixing at Downs at 1145 UTC is due to the arrival and impingement of a gravity current nose with the topography, it is possible to compare measurements with the theoretical trailing flow velocity u_g of gravity currents (Simpson 1999)

$$u_\mathrm{g} = \sqrt{gh\frac{\Delta T}{T_0}} \qquad (1)$$

where g is the gravitational acceleration, h the height of the gravity current, ΔT the temperature difference and T_0 the reference temperature. Figure 7c indicates $\Delta T \sim 4$ K, $T_0 = 288$ K, and using $h \sim 250$ m, it is possible to calculate $u_\mathrm{g} = 5.8$ m s^{-1}. This approximately agrees well with the observed gravity current trailing velocity of ~ 6 m s^{-1} (registered after 1145 UTC). As evident from Noh and Fernando (1991, 1993), the estimate (1) is only approximate, as other factors such as background turbulence and surface friction play a role in determining frontal propagation.

To reassert the gravity-current attributes of flow preceding the fog event, key meteorological parameters from a coastal buoy located north of St. Johns are shown in Fig. 9. Note the sudden drop of the temperature starting at 0630 UTC September 16 with a sharp

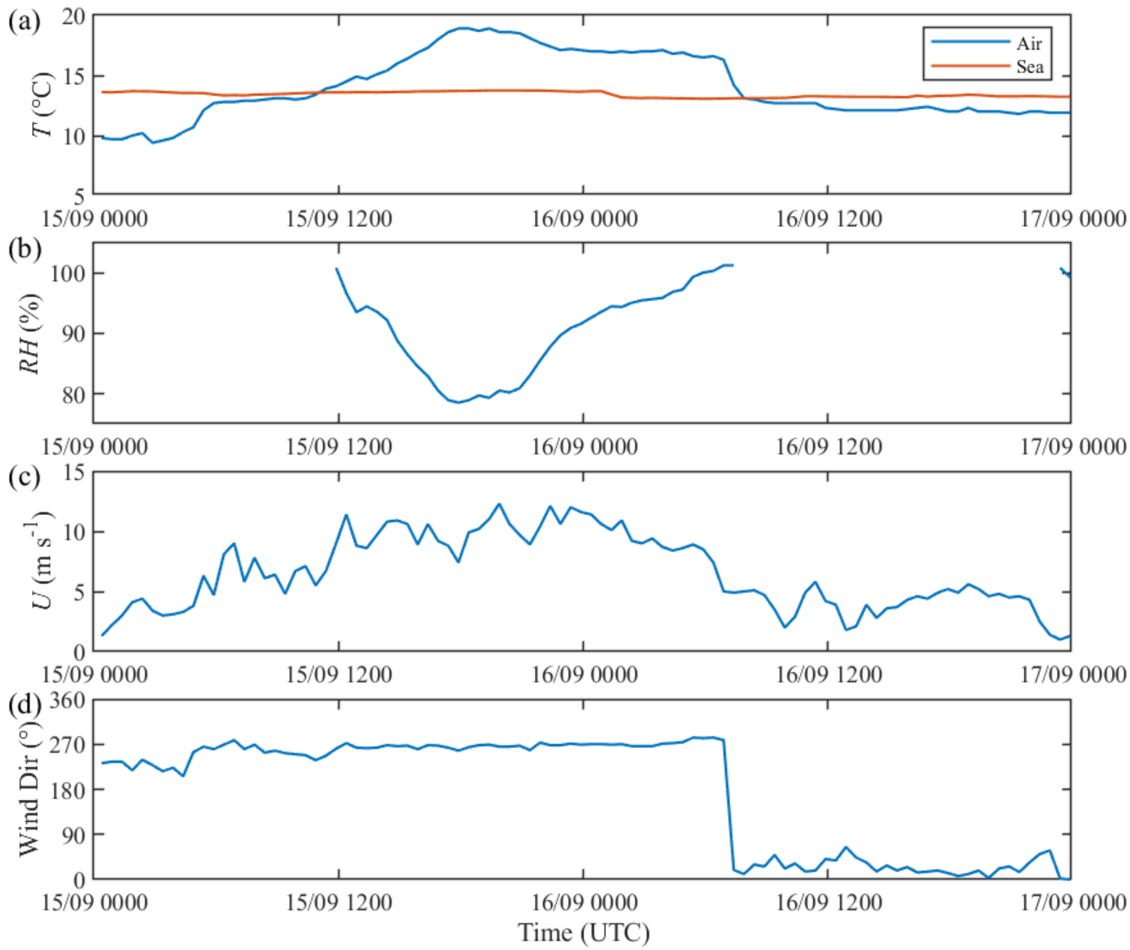

Fig. 9 Time series of (a) air and sea surface temperature, (b) relative humidity, (c) wind speed, and (d) wind direction recorded by a buoy located 6 km east of St. John's. The data was curated by the Smart Atlantic Alliance through the Memorial University of Newfoundland

change of wind direction from westerly to north-easterly and a drop of velocity to ~ 5 m s^{-1}, which can be identified with a south-westward propagating colder gravity current. If this current were to continue south-westward with a frontal flow velocity ~ 5 m s^{-1}, this gravity current is expected to arrive in Ferryland located ~ 60 km south of St. Johns within about 4.5 hours or around the observed time. The front is nearly saturated, and it arrival in Ferryland raises the relative humidity therein close to saturation following the mixing fog event.

The synoptic conditions surrounding the event are of interest, given our claim that a gravity-driven rather than a pressure-gradient driven flow is dominant after 1145 UTC. Figure 10 show synoptic maps of sea level pressure, 2-m air temperature, and 10-m wind

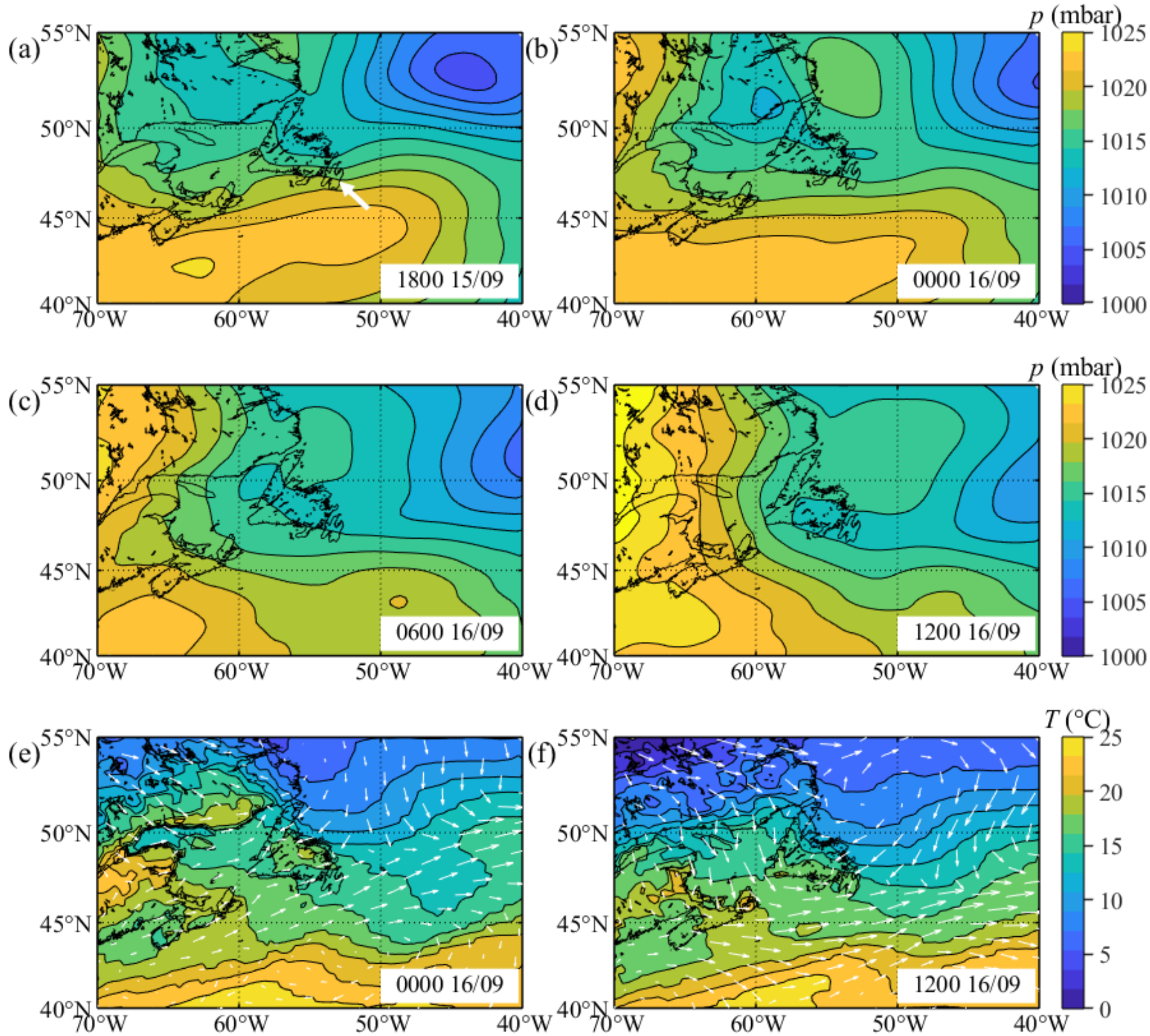

Fig. 10 NARR (a-d) sea level pressure plots and (e-f) 2 m air temperature and 10 m wind vectors for various dates. The time stamps are given in the plots. The white arrow in (a) points to Downs

vectors during IOP7, indicating an eastward moving Low about 5^{o} north of Ferryland (at ~ 53^{o} N) on September 15, consistent with the easterly flow observed before switching to northerly at 1130 UTC on 16 September. The low has cleared the general area by 1200 UTC 16 September, paving way to the north-easterly gravity current. Figure 10e,f shows that cold air in the wake of the Low is moving south-westward as a frontal system, undercutting warmer air, and its gravity driven nature is supported by (i) the broad agreement of flow velocity with the theoretical formula described above, and (ii) the southward propagation of cold air mass in the 2-m temperature maps of Fig. 10b that indicates ~ 16^{o}C air over Ferryland at 0000 UTC is replaced by ~ 12^{o}C air at around 1200 UTC.

After 1300 UTC, fog at Downs and Battery subsided, and the visibility gradually increased to ~10 km, but a strong fog presence was noted at the Judges Hill site where the visibility dropped to ~ 300 m and remained low until 2030 UTC, except for some sporadic (> 1 km) increases of visibility (Fig. 4a). This observation is consistent with the ceilometer observations of Fig. 4f that shows the development a stratus cloud layer shrouding the Judges Hill instrumentation (~129 m a.s.l.). This stratus-based fog development process is different from that at low levels, which is due to mixing induced by a gravity current impinging on the (Downs) topography. Prior to 1145 UTC September 16, the cloud base was too high (~200-250 m) for cloud-shrouding to affect visibility at the Judges Hill.

At Downs, from 1300 UTC until about 1400 UTC, there was an appreciable increase of the *TKE*, modest increase of σ_θ, and elevated level of *TKE* dissipation rate ε, pointing to turbulence in the trailing sheared gravity current. As mentioned, the drop of *T*, increase of *RH*, and a change of wind direction to a quasi-steady state indicate that at this time, the front has cleared the topography. In the trailing flow, the cloud layer is low, with its base at ~ 100 m (and the estimated cloud top at ~200-250 m), but the clouds stay clear from the ground. Between 1400 UTC and 1600 UTC, there is an increase of turbulence activity, possibly because of an increase of local wind speed. Intermittent stratus lowering occurred between 1530 and 1700 UTC, briefly enveloping Battery and Downs sites, as indicated in Fig. 4a,f, and observed from the camera (Fig. 5d). During this stratus lowering period, in general there were increased levels of *TKE*, ε, and σ_θ, pointing to enhanced turbulence responding to an increase of wind speed. At ~ 1700 UTC, the cloud layer started rising, even gradually clearing fog at Judges Hill. Complete clearing of fog at Judges Hill occurred after 2000 UTC, whence the base of the stratus cloud was about ~150 m. In all, local small-scale activities dominated Ferryland during and after fog/mist formation processes.

3 Laboratory Experiments

The laboratory experiments were directed at understanding the initial stages of the interaction of a gravity-current induced front with an obstacle to shed light on observations made during IOP7.

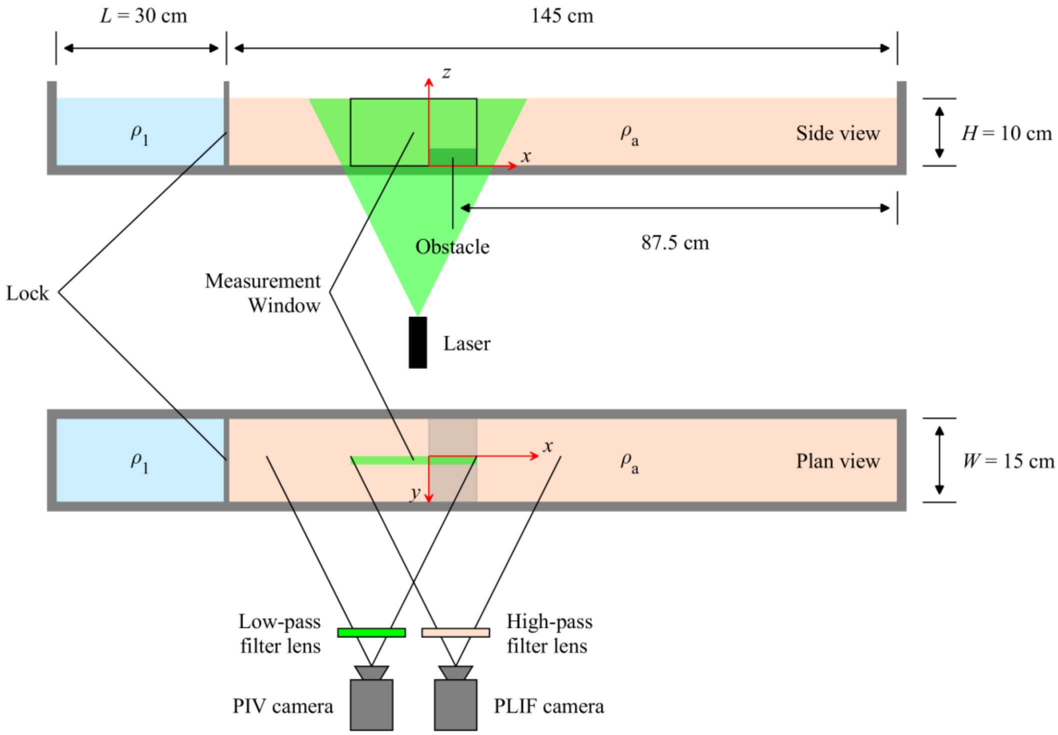

Fig. 11 The experimental setup for producing lock-exchange gravity currents. The gravity current was created by lifting the lock. PIV and PLIF techniques were used for flow diagnostics

3.1 Experimental (lock-exchange) configuration

The experiments were carried out in a 175 cm long, 15 cm wide, and 30 cm high Plexiglas tank. A gate (lock) was placed 30 cm from the left side of the tank that separated the dense fluid (density ρ_1) from the lighter fluid (ρ_a). The gravity current was generated by lifting the lock instantaneously. Figure 11 shows a schematic of the experimental configuration. A 1 W 520 nm continuous-wave diode laser was used to generate a laser sheet that illuminated the centre vertical section of the tank. The velocity and density fields were measured simultaneously using a time-resolved PIV/PLIF system. Two separate cameras were used for the particle image velocimetry (PIV) and planar laser-induced fluorescence (PLIF) measurements. The cameras were synchronized with a hardware trigger. Low- and high-pass filters (in wavelength) were mounted on the PIV and PLIF cameras to filter out unwanted signals.

Separate experiments were conducted with (obstructed) and without (unobstructed) topography. For obstructed runs, a 10 cm long and 2 cm high rectangular Plexiglas block that spans the tank width was placed at the centre of the tank. Ten independent replications were conducted with identical experimental parameters for each unobstructed and obstructed case to aid ensemble averaging. The fluid layer depth was $H = 10.0$ cm, which was selected to mimic the length scale ratio as in the field; for this case, the obstacle height to H ratio is 0.2, and in the field it is about 0.15. The dense fluid was prepared with a salt solution ($\rho_1 = 1002.3$ kg m^{-3}), and an aqueous ethanol solution with $\rho_a = 993.4$ kg m^{-3} was used as the lighter fluid. The densities were chosen such that the refractive indices between the two fluids are matched to prevent laser-beam distortions. The density and refractive indices were measured with a Mettler Toledo Densito 30 PX densitometer and a Leica handheld analogue refractometer. Hannoun et al. (1988), Strang and Fernando (2001), and Xu and Chen (2012) provide further details on the refractive-index matching technique.

3.2 Velocity measurements

Two-dimensional instantaneous velocity fields were obtained using high-frame-rate PIV. Both the dense and lighter fluids were seeded with hollow glass spheres with a median diameter of 10 µm. The 1 W 520 nm continuous-wave laser illuminated the particles. An IDS UI-3360CP-M USB 3.0 camera, equipped with a 2048 x 1088 pixels CMOS sensor and a 50 mm f/2.0 lens, was used at a frame rate of 40 Hz. A low-pass filter mounted on the lens filtered out the fluorescence of the PLIF dye from the laser light. The particle frames were processed using the MATLAB PIVlab package (Thielicke 2014; Thielicke and Stamhuis 2014; Thielicke and Stamhuis 2019), which is based on the iterative multigrid image deformation method (Scarano 2001). The sampling frequency and interrogation window size were chosen such that they met the one-quarter rule (Adrian 1991). Consequently, the window size of the final selection was 16 x 16 pixels with a 50% overlap.

3.3 Density measurements

Time-resolved PLIF measurements provided density fields within gravity currents. Rhodamine 6G (R6G) was chosen as the fluorescent dye because of its high quantum efficiency, high resistance to photo-bleaching, and because its absorption peak of 525 nm (Crimaldi 2008) is close to the laser wavelength (520 nm). The dye was added only to the lighter fluid at an initial concentration of 100 µg L^{-1}. The fluorescence intensity was recorded by an IDS uEye UI-1220-C USB 2.0 camera with a 752 x 480 pixels CMOS sensor. A high-pass filter with a cut-off wavelength of 550 nm was mounted on the PLIF camera lens to filter out the laser light. The majority of the fluorescence was retained because the fluorescence spectrum of R6G has a peak at 555 nm (Penzkofer and Leupacher 1987). The R6G concentrations were calculated from the grey values using the calibration technique described by Xu and Chen (2012). Local density values were derived from the measured R6G concentration using a calibration curve.

3.4 Phase-aligned ensemble averaging technique

Turbulence statics of obstructed and unobstructed gravity currents were obtained by ensemble averaging because of the nonstationarity and spatial inhomogeneity of gravity currents. Similar to Zhong et al. (2018, 2020), we applied the phase-aligned ensemble averaging technique (PAET), which aligns the time and space coordinates of each realization to minimize jitter. It iteratively maximizes the cross-correlation of individual realizations with the ensemble-averaged field by shifting the realizations along space and time axes. In this study, the alignment was only necessary for time since the horizontal variations are fixed by the position of the obstacle (or centre of the tank), and vertical variations are limited by the tank bottom and the water surface. More details of PAET as applied to gravity currents are given in Zhong et al. (2020).

4 Observations

4.1 Observations of obstructed gravity currents

The gravity current, formed after lifting the lock, propagated towards the obstacle and impinged on it. An example of the instantaneous normalized density field of an obstructed run is shown in Fig. 12. Based on the horizontal frontal velocity u_F the flow could be divided into four stages. In the first stage, the gravity current propagated independently of the obstacle at a constant speed. In stage two, as the gravity current approached the obstacle,

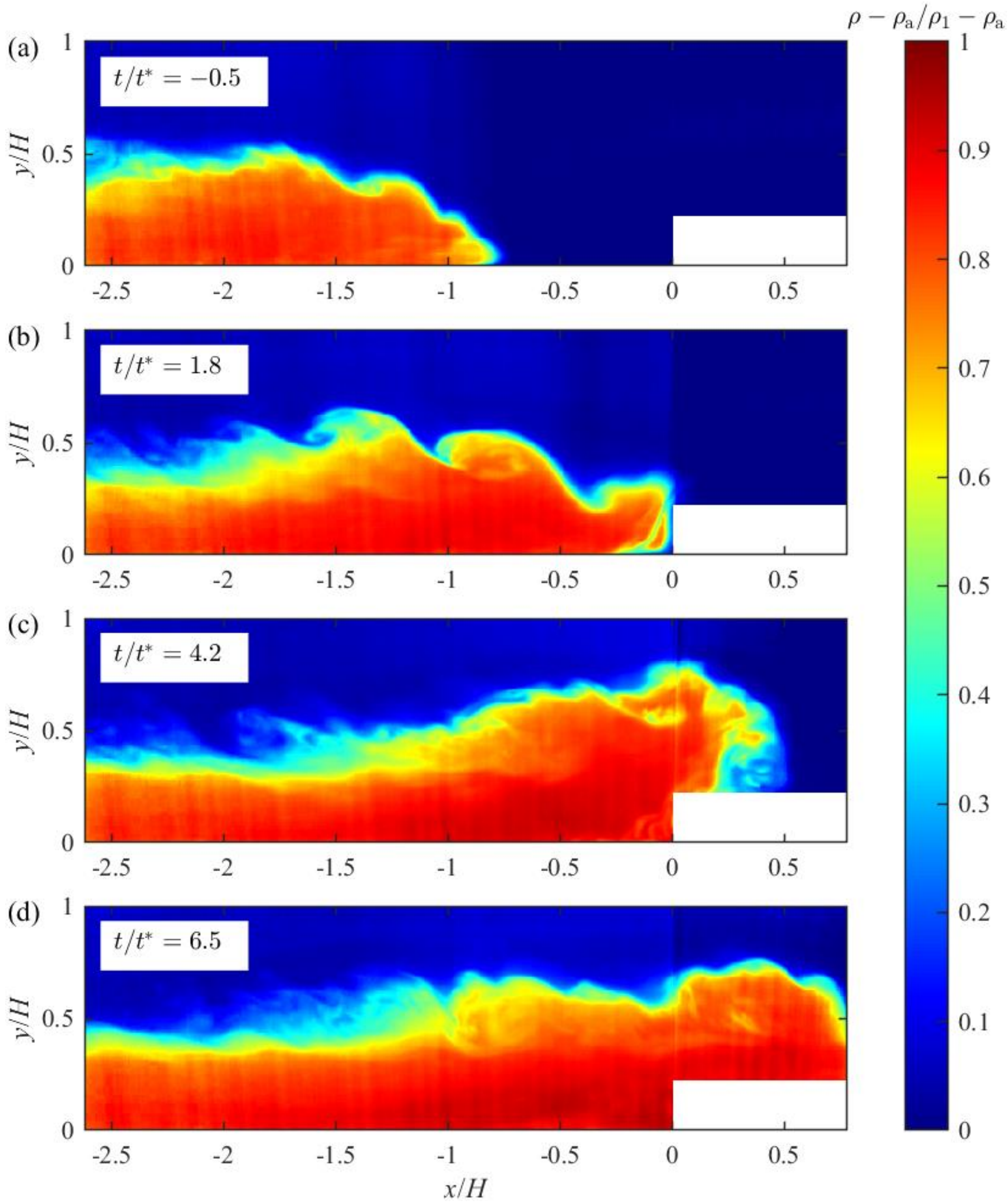

Fig. 12 The instantaneous normalized density field for an obstructed run. The time origin is set to the instance where the gravity current makes contact with the obstacle

the horizontal front velocity gradually decreased with time. The collision of the gravity current with the obstacle is the third stage, which is characterized by a low horizontal frontal velocity and near stagnation. A part of the current deflected vertically similar to a jet, reaching a maximum height of about 0.8H. A vortex was formed at the leading edge of the obstacle that provided enhanced mixing. The current was also partially reflected as a hydraulic jump moving upstream. At the start of the fourth stage, the gravity current collapsed and continued to propagate over the obstacle.

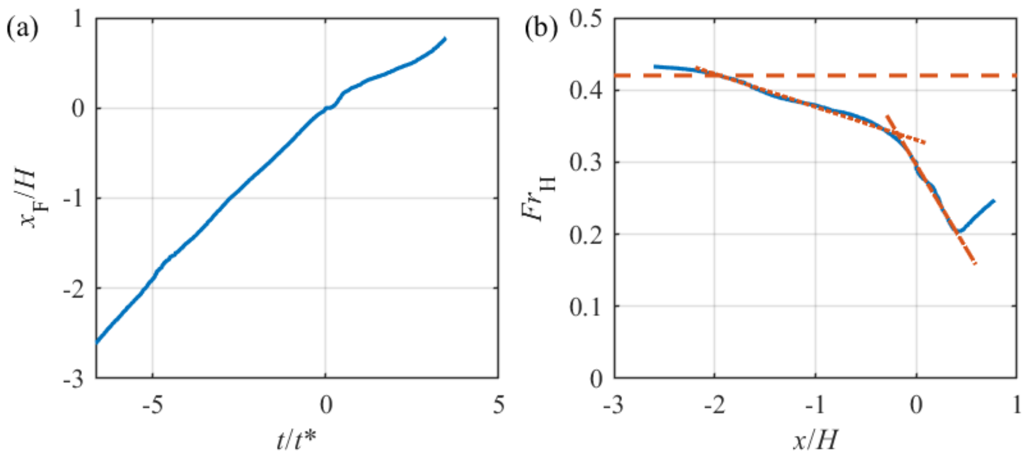

Fig. 13 Propagation of the gravity current toward the obstacle, with (a) normalized frontal position as a function of time and (b) normalized frontal velocity as a function of normalized frontal position (show by lines, the different phases). The dashed lines indicate various phases of propagation described in the text. For this experiment, $\rho_1 = 1002.3$ kg m^{-3}, $\rho_a = 993.4$ kg m-3, and $H = 10$ cm

According to the hydraulic (inviscid) analysis of Benjamin (1968), an unobstructed gravity current in its energy conserving mode has a height of $h_g = 0.5H$ and a Froude number of $Fr_H = \frac{u_F}{\sqrt{g'H}} = 0.5$, where u_F is the frontal velocity, $g' = g(\rho_1 - \rho_a)/\rho_0$ the reduced gravity, and $\rho_0 = (\rho_1 + \rho_a)/2$ is a reference density. Previous laboratory and numerical experiments have shown that in practice Fr_H has values between 0.36 and 0.45 for gravity currents produced by lock-exchange (Zhong et al. 2018). In the present unobstructed experiments, it was found that $Fr_H \approx 0.42$, which agrees well with the observation that gravity currents, after their initial development, typically have a constant velocity for about 5-10 lockbox lengths L (Meiburg and Kneller 2010). This is called the slumping phase. In our case, the obstacle is located $3L$ from the lock, and hence observations are in the slumping phase. Figure 13 shows ensemble-averaged results for a run, where the normalized frontal position x_F relative to the obstacle leading edge (x = 0) is shown as a function of time. Here x_F was measured using PLIF by locating the largest x-value of the $\rho^* = (\rho - \rho_a)/(\rho_1 - \rho_a) = 0.1$ contour.

The normalization variables were selected based on the intrinsic velocity, length, and time scales of unobstructed runs: $\sqrt{g'H}$, H and $t^* = \sqrt{H/g'}$, respectively. Note that near the obstacle the horizontal frontal speed is significantly reduced (Fig. 13a,b) as the front is deflected upward and start overrunning the obstacle (Fig. 12c,d).

The Froude number Fr_H can be interpreted as a measure of the ratio of the kinetic energy of fluid parcels at the gravity current front ($\sim u_F^2$) to the potential energy acquired by their rise over the height of the current ($\sim g'H$) (c.f., Lane-Serff et al. 1995). Fr_H is an important quantity in specifying an unobstructed gravity current, but when it interacts with an obstacle an additional parameter $1/G = u_F/\sqrt{g'd} = Fr_H\left(\sqrt{H/d}\right)$ becomes important (d being the obstacle height). In general, the interaction between a gravity current and a 2D obstacle is a multi-parameter problem, determined by upstream Fr_H, d/H and other geometric ratios; for discussions, see Baines (1998) and Vassallo et al. (2021). The variation of Fr_H as a function of the front position x_F/H is shown in Fig. 13b, where in the unobstructed phase the Froude number maintains an approximately constant value of $Fr_H = 0.42$ until the gravity current is at a distance $2H$ away from the obstacle (i.e., the first stage). As mentioned, this is valid for all runs conducted. The flow evolution beyond the first stage is expected to be determined by additional parameters such as d/H.

As evident from Fig. 13b, during the second stage, the Froude number based on local u_F slowly decreases with time to about 0.35, and this upstream influence is due to stronger return flows established in the proximity of the obstacle. When the gravity current collides with the obstacle in stage three, Fr_H decreases significantly to a minimum value of 0.2 or $G \approx 0.45$. The decrease is associated with the vertical deflection of the gravity current during the collision. The Froude number slowly increases again as the gravity current continues to propagate over the obstacle, after adjusting to the new propagation state. Given the interest of this paper is mixing during the collision stage, detailed studies were not conducted on how local Fr_H varies with d/H and other geometric parameters or the properties of the layer overflowing or reflected back from the obstacle.

4.2 Mixing

To quantify enhanced mixing at the obstacle between the gravity current front and background fluid, the variability of mixed fluid volume was measured. Given the high space-time variability and steep concentration gradients involved, direct measurements of

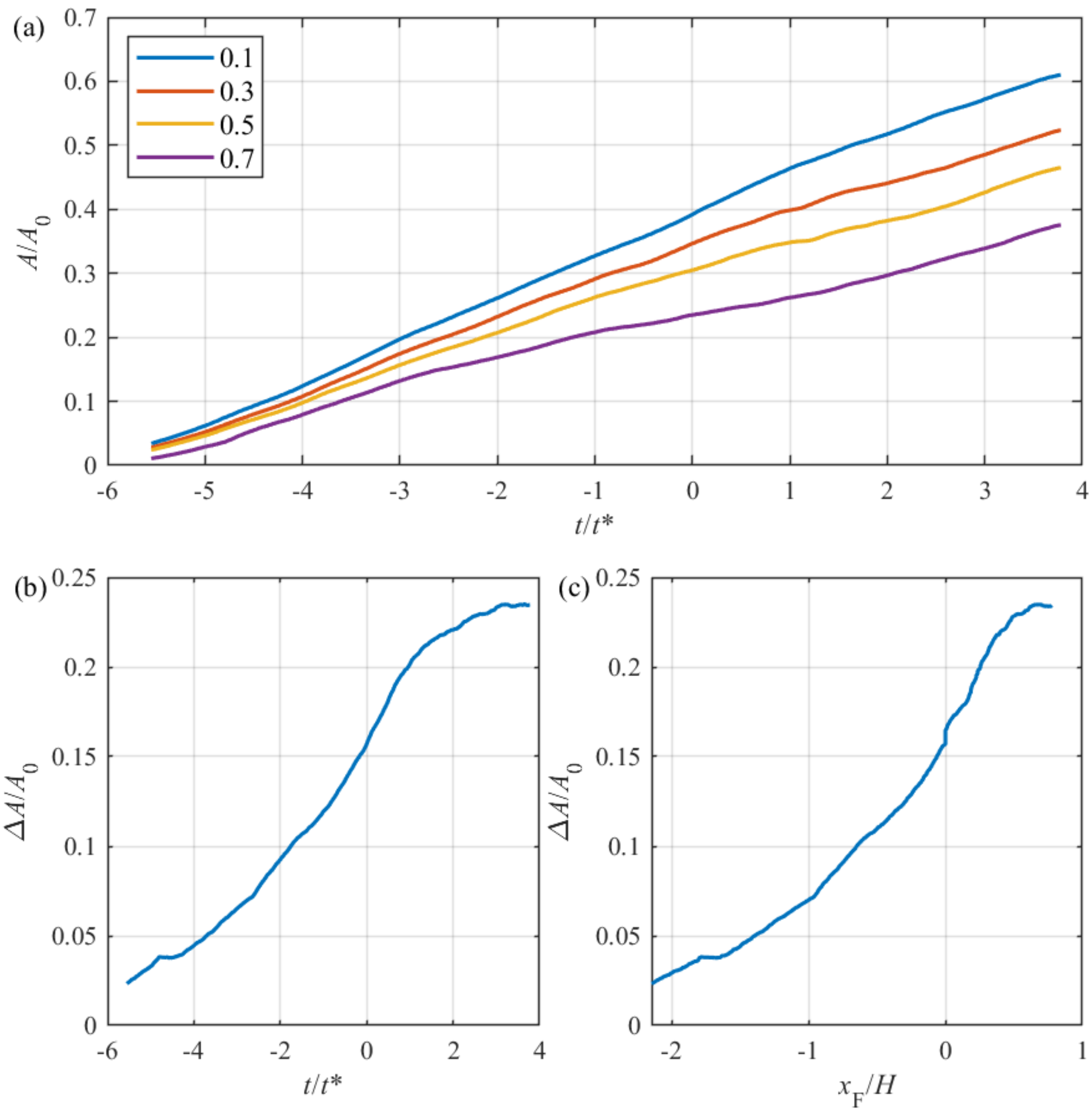

Fig. 14 Time series of (a) four different isopleths; (b) the difference of $\rho^* = 0.1$ and $\rho^* = 0.7$ isopleths as a function of normalized time; (c) the difference of the $\rho^* = 0.1$ and $\rho^* = 0.7$ isopleths as a function of normalized frontal position x_F/H

molecular-scale mixing rates (or dissipation rates of a scalar) are untenable with the resolution of the current (and other available) techniques, but the amount of mixed fluid present can be quantified in an integral sense by measuring the time evolution of the density field over the domain of the gravity current. In our case, because of the limited field of view, it was not possible to probe the entire gravity current, but a sound quantitative estimate of mixing could be obtained by considering the time evolution of mixed fluid within the field of view. Figure 14a shows the normalized volumes of 'mixed' fluid per unit tank width, where A_0 is the volume per tank width of the measurement window excluding the obstacle and A the volume per tank width of fluid parcels with a density at or above a given density threshold. The density thresholds in Fig. 14a are $\rho^* = (\rho - \rho_a)/(\rho_1 - \rho_a) = 0.7$, 0.5, 0.3, and 0.1. Curves for a given ρ^* threshold will be referred to as an isopleth. Note that the fractional area A/A_0 of the isopleths increases with time because more gravity current fluid is arriving in the field of view. If no further mixing takes place in the field of view, then the fraction A/A_0 ought to increase linearly with time t (i.e., dA/dt is constant) in Stage 1, given the constant speed of the gravity current feeding the mixing area. When mixing takes place, dA/dt is also dependent on the rate of mixing, whence fluid with lesser densities are generated due to mixing.

As pointed out by Hacker et al. (1996), mixing in a flow can be quantified by considering the evolution of isopleths. That is, the volume of fluid for a given normalized density range can be reckoned by subtracting the A/A_0 values corresponding to two isopleths. This is illustrated in Fig. 14b,c for temporal and spatial characteristics. For example, the volume of mixed fluid in the range of $0.1 \le \rho^* < 0.7$ can be found by taking the difference of A/A_0 values of 0.1 and 0.7 isopleths, with the divergence of two isopleths being an indicator of how the density distribution changed due to mixing by reducing the A/A_0 ratio corresponding to the $\rho^* = 0.7$ and increasing that of the $\rho^* = 0.1$ isopleth. In order to quantify the mixing, we will focus on the divergence of the $\rho^* = 0.1$ and 0.7 isopleths, $\Delta A/A_0$ by taking the difference of A/A_0 at a given instant. In Fig. 14 until $t/t^* \approx -1.5$ the rate of increase of $\Delta A/A_0$ is approximately constant. Between $t/t^* \approx -1.5$ and $t/t^* \approx 1.5$, the divergence of the isopleths increases significantly faster with time (Figs. 14b,c), which coincides with the arrival of the front at the obstacle (Stage 3) wherein mixing enhances due to the collision of the gravity current with the topography at $t/t^* = 0$. After $t/t^* \approx 1.5$ the divergence decreases again, and thus there is less mixing taking place.

The period $\Delta t/t^*$ where enhanced mixing takes place can be evaluated by finding the period beyond which the slope of $\Delta A/A_0$ drops to half of its maximum. When applied to Fig. 14, its normalized value could be evaluated as $\Delta t/t^* \approx 3$. This period corresponds to frontal positions over the range $-0.5 < x/H < 0.33$, which surrounds the leading edge of the obstacle. These temporal and spatial scales of enhanced mixing, when applied to IOP7, yield a duration of ~ 2.8 min over a length of ~ 400 m for $H = 2h_g = 450$ m, $g' = 0.15$ m s^{-2}. This indicates that scalar (water vapour and temperature) mixing is permeated to molecular scales quite rapidly after large-scale turbulence is generated by impingement of gravity current on the topography, thus facilitating the activation of condensation nuclei within the smallest scales of turbulence (i.e., Kolmogorov scale) and appearance of fog over a short time scale. According to Fernando and Hunt (1996), the time scale for homogenization when two dissimilar concentrations are bought together in a turbulent fluid is ℓ/σ , where ℓ is the integral length scale and σ the *rms* velocity of turbulence. For the case of Downs topography, this can be estimated using ℓ = 30 m and $\sigma = \sqrt{TKE}$ ~ 0.2 m s^{-1} as 2.5 min, which is in broad agreement with the laboratory-based estimates presented above. Note that the gravity current front approaches Downs topography at ~1130 UTC (Fig. 7a-d), mixing becomes intense at ~1200 UTC (Fig 7e-h) and we expect the fog to appear soon thereafter.

5 Discussion

The laboratory experiment described above was intended to provide physical insights and relevant scales pertinent to gravity-current/topography interactions. In the traditional (reductionist) approach to modelling, the study of complex natural flows is made tractable by employing simplified yet realistic geometries in designing model configurations. In our case, the long narrow stretch of Downs peninsula with a 'tadpole' headland (Fig. 2) was approximated by a two-dimensional topography with a rectangular cross section, the approach flow being normal to the long axis, notwithstanding in reality the approach flow is about 45^{o} to the long axis. The laboratory working fluid was water, which has been a customary working fluid in previous laboratory simulations of atmospheric flows. In particular, Chen et al. (1996, 1999) showed that the equations for the conservation of momentum, mass, and buoyancy in a water-tank model are similar to those in the atmosphere: the counterparts of the potential temperature and Exner function in the atmosphere correspond to the specific volume and pressure, respectively, of the experimental fluid (also see Berman et al. 1995). The displacements, velocity, and temperature fields play similar roles in the atmosphere and in the model. Therefore, with suitable matching of dimensionless parameters, it is possible to mimic natural flow processes using water tank experiments.

For the laboratory case of Fig. 11, the governing variables are g', H, the width w_0 and the height d of the obstacle, and the kinematic viscosity ν of the working fluid. The ratios d/w_0 and d/H were maintained at 0.2, close to that of Downs topography 0.15. With some manipulation, the frontal velocity of the gravity current prior to the influence of the obstacle and away from the lock can be written as $u_{\mathrm{F}}/\sqrt{g'H} = \Psi(Re)$,where $Re = u_F H/\nu$ can be construed as the Reynolds number. Independence on the Reynolds number (or the Reynolds number similarity; Barenblatt 1996) applies at high Re, whence $u_{\mathrm{F}} = C\sqrt{g'H}$, where C is a constant. Previous and current experiments show a constant $C =$ 0.36-0.45, implying Reynolds number similarity. The value of Re for the current experiments is about 9300 whereas for IOP7 $Re \sim 10^9$. Breidenthal (1981) proposed that Reynolds-number independent mixing is achieved when $Re > 3000$, an aspect that has been further discussed by Princevac et al. (2005) and Zhong et al. (2018). Given both laboratory and field Re are greater than the critical value above, we may assume that our laboratory experiments can provide useful information on mixing in natural gravity currents. It is also noted that the highest achievable Reynolds numbers in lock-exchange laboratory tanks are of the order $(10^3 - 10^5)$.

Worthy of mentioning are the shallow water models and high-resolution numerical simulations on gravity/turbidity currents propagating past topographies, for which substantial literature exists. Layered (1.5, 2, and 2.5) shallow water models have been developed and refined since Rottman et al. (1985) to describe the approach, overflow and reflected phases (Lane-Serff et al. 1995), but these models cannot capture the initial impact and vertical flow deflection let alone mixing down to dissipation scales. Direct numerical simulation (DNS) and Large-Eddy Simulation (LES) of lock-exchange (e.g., Gonzalez-Juez and Meiburg 2009; Gonzalez-Juez et al. 2009; Nasr-Azadani et al. (2014, 2018) using DNS; and Tokay and Constantenescu 2015; Bhaganagar 2017; Zhou and Venayagamoorthy 2017; Wu and Ouyang 2020 using LES) and steady constant flux (Tokay and Constantinescu (2015) using LES) gravity and turbidity currents interacting with obstacles have been reported, with identification of fine-scale details of flow evolution around the obstacle. These studies, however, did not identify the time scale of scalar mixing (homogenization at small scales) that is interest to our study, which was prompted by the field observations.

6 Conclusions

An interesting short-lived mixing-fog event occurred during the IOP7 of the C-FOG project, where a cold front arriving from the north-east collided on the Downs peninsula to produce foggy/misty conditions. The collision caused turbulent mixing of nearly saturated ambient air with the almost saturated cold front, creating fog. The conditions were such that fog lasted for a short period of time, and the final mixture of airmasses quickly reached the unsaturated region of the vapour pressure/temperature diagram.

Earlier in the day, the conditions were clear at the three Ferryland sites until 1200 UTC, whence visibilities fluctuated and dropped < 1 km at the low-lying stations. At the same time, the liquid water content, droplet number concentration, mean diameter, and total aerosol count increased. The tower data showed a drop of temperature, an increase of relative humidity, and an increase of *TKE* and its dissipation rate, and *rms* temperature fluctuations. These observations suggest the possibility of a local turbulent mixing event triggered by topographically induced mixing of two nearly saturated air masses with different temperatures that led to fog. Measurements of a Sodar/RASS system, a meteorological flux tower, a meteorological buoy located ~ 60 km upstream and synoptic weather maps gave perspectives of the cold front. They pointed to a shallow gravity current nose with a trailing current of about 200-250 m high arriving prior to the fog event. This was confirmed by a radiosonde launch that followed. The observed velocity of the trailing current agreed with the theoretical velocity.

Motivated by these observations, laboratory experiments were performed to study the interaction of gravity currents with a rectangular obstacle to confirm enhanced mixing at the topography as well as quantify the timescale for molecular-scale mixing due to the collision (which is representative of the time for fog appearance following condensation nuclei activation). Gravity currents were generated by lifting a (proverbial) lock that separated a dense saline solution from a lighter ethanol solution that served as the ambient fluid. The refractive index matching of the fluids made it possible to use optical techniques for flow diagnostics. Instantaneous velocity and density fields were measured simultaneously using PIV/PLIF techniques. Molecular-level mixing was quantified by considering the divergence of a set of concentration isopleths. Given the logistical constraints, the ratios of the obstacle height to the fluid layer depth and the aspect ratio of the obstacle were kept fixed in the experiments reported in this paper, approximately matched with the field conditions. Future studies ought to study the effect of these parameters.

The propagation of the obstructed gravity current and its interaction with the obstacle during experiments could be divided into four stages, namely, propagation independent of the obstacle, approach, collision and continued propagation. Most of the mixing occurs in the third stage due to turbulent eddies (vertical structures) generated during the collision. An analysis based on isopleths confirmed increased (molecular-scale) mixing during the collision, with enhanced mixing starting at $t/t^* = -1.5$ and reaching a maximum at $t/t^* = 1.5$, and decreasing rapidly thereafter. The period of enhanced mixing was $\Delta t/t^* \approx 3$ and the extent around the obstacle that showed increased mixing was $-0.5 < x_F/H < 0.33$. When applied to the IOP7 case, the time scale and length scale of enhanced mixing were ~ 2.8 min and ~ 400 m, respectively. The smaller space-time scales involved in the natural fog situation studied in this paper points to the difficulty of simulating mixing fog using mesoscale numerical weather prediction (NWP) models, since critical underlying processes of fog formation belong to the sub-grid category. The success of fog predictions in NWP models, therefore, is expected to be sensitively dependent on the efficacy of sub-grid parameterizations.

Acknowledgements This research was funded by the Office of Naval Research Award # N00014-18-1-2472 entitled: Toward Improving Coastal Fog Prediction (C-FOG). We would like to thank Scott Coppersmith and Joo Sung Kim for their help with the laboratory experiments. The microphysical data were obtained from the Naval Postgraduate School group led by Professor Qing Wang, with Dr. Denny Allapattu and Mr. Ryan Yamaguchi making contributions. We also thank Dr. Ismail Gultepe, Sandeep Wagh and Mr. Sen Wang for their help in numerous ways.

References

Adrian RJ (1991) Particle-imaging techniques for experimental fluid mechanics. Annu Rev Fluid Mech 23(1):261-304

American Meteorological Society (2020) Fog. (Available online at http://glossary.ametsoc.org/wiki/fog)

Baines PG (1998) Topographic Effects in Stratified Flows. Cambridge University Press, Cambridge, UK

Barenblatt GI (1996) Self-Similarity, and Intermediate Asymptotics: Dimensional Analysis and Intermediate Asymptotics. Cambridge University Press

Benjamin TB (1968) Gravity currents and related phenomena. J Fluid Mech 31(2):209-248

Berman NS, Boyer DL, Brazel AJ, Brazel SW, Chen, RR, Fernando HJS, Fitch MJ (1995) Synoptic classification and physical model experiments to guide field studies in complex terrain. J Appl Meteorol 34:719-730

Bhaganagar K (2017) Role of head of turbulent 3-d density currents in mixing during slumping regime. Phys of Fluids 29(2):020-703

Breidenthal R (1981) Structure in turbulent mixing layers and wakes using a chemical reaction. J Fluid Mech 109:1-24

Byers HR (1959) General Meteorology, 3rd edn. McGraw Hill, New York

Chen RR, Berman NS, Boyer DL, Fernando HJS (1996) Physical model of diurnal heating in the vicinity of a two-dimensional ridge. J Atmos Sci 53:62-85

Chen RR, Berman NS, Boyer DL, Fernando HJS (1999) Physical model of nocturnal drainage flow in complex terrain. Contr. Atmos. Phys., 72, 219-242

Crimaldi JP (2008) Planar laser induced fluorescence in aqueous flows. Exp Fluids 44(6):851-863

Fernando HJS, Hunt JCR (1996) Some aspects of turbulence and mixing in stably stratifed layers. Dyn Atmos Oceans 23(1-4):35-62

Fernando HJS, Gultepe I, Dorman C, Pardyjak E, Wang Q, Hoch SW, Richter D, Creegan E, Gaberšek S, Bullock T, Hocut C, Chang R, Alappattu D, Dimitrova R, Flagg D, Grachev A, Krishnamurthy R, Singh DK, Lozovatsky I, Nagare B, Sharma A, Wagh S, Wainwright C, Wroblewski M, Yamaguchi R, Bardoel S, Coppersmith RS, Chisholm N, Gonzalez E, Gunawardena N, Hyde O, Morrison T, Olson A, Perelet A, Perrie W, Wang S, Wauer B (20210) C-fog: Life of coastal fog. Bull Am Meteorol Soc. https://doi.org/10.1175/BAMS-D-19-0070.1

George JJ (1940) Fog: Its causes and forecasting with special reference to eastern and southern united states (i). Bull Am Meteorol Soc 21(4):135-148

Gonzalez-Juez E, Meiburg E, Constantinescu G (2009) Gravity currents impinging on bottom-mounted square cylinders: flow fields and associated forces. J Fluid Mech 631:65-102

Gonzalez-Juez E, Meiburg E (2009) Shallow-water analysis of gravity-current flows past isolated obstacles. J Fluid Mech 635:415-438Goodman J (1977) The Microstructure of California Coastal Fog and Stratus. J Appl Meteorol 16:1056-1067

Grachev AA, Leo LS, Fernando HJS, Fairall CW, Creegan E, Blomquist BW, Christman AJ, Hocut CM (2018) Air-sea/land interaction in the coastal zone. Boundary-Layer Meteorol. 167(2): 181–210. https://doi.org/10.1007/s10546-017-0326-2

Grachev AA, Krishnamurthy R, Fernando HJS, Fairall CW, Bardoel SL, Wang S (2021) Atmospheric turbulence measurements at a coastal zone with and without fog. Boundary-Layer Meteorol (submitted)

Gultepe I, Tardif R, Michaelides SC, Cermak J, Bott A, Bendix J, Müller MD, Pagowski M, Hansen B, Ellrod G, Jacobs W, Toth G, Cober SG (2007) Fog research: A review of past achievements and future perspectives. Pure Appl Geophys 164(6-7):1121-1159

Hacker J, Linden PF, Dalziel SB (1996) Mixing in lock-release gravity currents. Dyn Atmos Oceans 24(1-4):183-195

Hannoun IA, Fernando HJS, List EJ (1988) Turbulence structure near a sharp density interface. J Fluid Mech 189:189-209

Hunt JCR, Pacheco JR, Mahalov A, Fernando HJS (2005) Effects of rotation and sloping terrain on the fronts of density currents. J Fluid Mech 537:285-315

Jung JH, Yoon HS (2016) Effect of scour depth on flow around circular cylinder in gravity current. Ocean Engineering 117:78-87

Lane-Serff GF, Beal LM, Hadfield TD (1995) Gravity current flow over obstacles. J Fluid Mech 292:39-53

Mahalov A, Pacheco JR, Voropayev SI, Fernando HJS, Hunt JCR (2000) Effects of rotation on fronts of density currents. Physics Letters A 270(3-4):149-156

Meiburg E, Kneller B (2010) Turbidity currents and their deposits. Annu Rev Fluid Mech 42:135-156.

Nasr-Azadani MM, Meiburg E (2014) Turbidity currents interacting with three-dimensional seafloor topography. J Fluid Mech 745:409-443.

Nasr-Azadani MM, Meiburg E, Kneller B (2018) Mixing dynamics of turbidity currents interacting with complex seafloor topography. Environ Fluid Mech 18(1):201-223

Newsom RK, Krishnamurthy R (2020). Doppler Lidar (DL) instrument handbook. DOE ARM Climate Research Facility, Tech. Rep. DOE/SC-ARM-TR-101

Noh Y, Fernando HJS (1991) Gravity current propagation along an incline in the presence of boundary mixing. J Geophys Res 96(C7):12586-12592

Noh Y, Fernando HJS (1993) A numerical model of the fluid motion at a density front in the presence of background turbulence. J Phys Ocean, 23(6):1142-1153

Paoli R, Shariff K (2016) Contrail modeling and simulation. Annu Rev Fluid Mech 48:393-427

Penzkofer A, Leupacher W (1987) Fluorescence behaviour of highly concentrated rhodamine 6G solutions. Journal of Luminescence 37(2):61-72

Petterssen S (1941) Recent fog investigations. Journal of the Aeronautical Sciences 8(3):91-102

Roach WT (1994) Back to basics: Fog: Part 1 - definitions and basic physics. Weather London 49:411-415

Rodhe B (1962) The effect of turbulence on fog formation. Tellus 14(1):49-86

Rottman JW, Simpson JE, Hunt JCR (1985) Unsteady gravity current flows over obstacles: some observations and analysis related to the phase II trials J Hazard Mater 11:325–340

Princevac M, Fernando HJS, Whiteman CD (2005) Turbulent entrainment into natural gravity-driven flows. J Fluid Mech 533:259-268

Scarano F (2001) Iterative image deformation methods in PIV. Measurement science and technology 13(1):R1

Schumann U (1996) On conditions for contrail formation from aircraft exhausts. Meteorol Z 5:4–23

Simpson JE (1999) Gravity currents: In the environment and the laboratory. Cambridge university press

Strang EJ, Fernando HJS (2001) Entrainment and mixing in stratified shear flows. J Fluid Mech 428:349-386

Taylor GI (1917) The formation of fog and mist. Q J R Meteorol Soc 43(183):241-268

Thielicke W (2014) The flapping flight of birds: Analysis and application. PhD thesis, University of Groningen

Thielicke W, Stamhuis E (2014) PIVlab - towards user-friendly, affordable and accurate digital particle image velocimetry in MATLAB. Journal of Open Research Software 2(1)

Thielicke W, Stamhuis EJ (2019) PIVlab - time-resolved digital particle image velocimetry tool for matlab

Tokyay T, Constantinescu G (2015) The effects of a submerged non-erodible triangular obstacle on bottom propagating gravity currents. Phys Fluids 27(5):056-601

Tokyay T, Constantinescu G, Meiburg E (2012) Tail structure and bed friction velocity distribution of gravity currents propagating over an array of obstacles. J Fluid Mech 694:252-291

Vassallo D, Krishnamurthy R, Menke R, Fernando, HJS (2021) Observations of stably stratified flow through a microscale gap. J Atmos Sci, 78(1):189-208

Wilson RI, Friedrich H, Stevens C (2018) Flow structure of unconfined turbidity currents interacting with an obstacle. Environ Fluid Mech 18(6):1571-1594

Wilson RI, Friedrich H, Stevens C (2019) Quantifying propagation characteristics of unconfined turbidity currents interacting with an obstacle within the slumping regime. Journal of Hydraulic Research 57(4):498-516.

Wu CS, Ouyang HT (2020) Flow morphology in bottom-propagating gravity currents over immersed obstacles. AIP Advances 10(11):115103

Xu D, Chen J (2012) Experimental study of stratified jet by simultaneous measurements of velocity and density fields. Exp Fluids 53(1):145-162

Zhong Q, Hussain F, Fernando HJS (2018) Quantification of turbulent mixing in colliding gravity currents. J Fluid Mech 851:125-147

Zhong Q, Hussain F, Fernando, HJS (2020) Application of Phase Averaging to Investigate Spasmodic Mixing in Environmental Flows. Journal of Environmental Fluid Mechanics 20:1357–1377

Zhou J, Venayagamoorthy SK (2017) Numerical simulations of intrusive gravity currents interacting with a bottom-mounted obstacle in a continuously stratified ambient. Environ Fluid Mech 17(2):191-209